applied sciences

MDPI

Article

Research on the Sound Absorption Performance of Porous Asphalt Concrete with Different Air Voids Based on the Finite Element Models

Jianguang Xie, Yiwei Zhu and Zhanqi Wang *

Department of Civil and Airport Engineering, Nanjing University of Aeronautics and Astronautics, Nanjing 211106, China
* Correspondence: wangzq911201@nuaa.edu.cn

Abstract: This paper aims to investigate the effect of the void structure of porous asphalt concrete (PAC) on the sound absorption performance. The sound absorption coefficient (SAC) spectra of PAC with various voids were measured using the transfer function method and the air void structure was identified from Computed Tomography (CT) scanning images. The finite element model (FEM) of the void structure was established via CT cross-sectional images to research the noise reduction mechanism of PAC. At different frequencies, the sound pressure level distribution and SAC were calculated. The following are the main conclusions: (1) As the void content of PAC increases, the SAC spectrum curve becomes higher, more rightward and wider, while the peak values, their corresponding frequencies and mean values increase. (2) The SAC decreases with the average number of voids within each image and increases with the void equivalent diameter and fractal dimension; there exist linear relationships between these three parameters and the SAC. (3) The sound absorption capacity of the void with larger size and fractal dimension is higher than the smaller one and the voids connected to the upper and lower surfaces provide more noise reduction. (4) The FEMs of PAC can predict the SAC of PAC.

Keywords: porous asphalt concrete; sound absorption coefficients; microscopic void structure; FEM; noise reduction mechanism

Citation: Xie, J.; Zhu, Y.; Wang, Z. Research on the Sound Absorption Performance of Porous Asphalt Concrete with Different Air Voids Based on the Finite Element Models. *Appl. Sci.* **2022**, *12*, 11050. https://doi.org/10.3390/app122111050

Academic Editors: Jiaqi Chen, Kezhen Yan and Jun Xie

Received: 4 October 2022
Accepted: 27 October 2022
Published: 31 October 2022

1. Introduction

Road traffic has been rapidly developed in the past decades. However, traffic noise pollution has endangered the physical and emotional health of drivers and inhabitants near roads. Long-term exposure to noise may even cause health issues including tinnitus and hypertension [1].

Common methods for reducing road noise include installing sound barriers, planting green belts, and constructing porous asphalt pavements. However, there are some shortcomings with the first and second methods, such as more time and money are needed. At the annual meetings of the Transportation Research Board (TRB), many opinions were shared to deal with the traffic noise problems [2–4]. It is widely recognized that aiming at the PAC design is better than the research on tire structure because the former costs less and still has massive noise reduction.

Therefore, many road engineers have focused on porous asphalt pavements. Porous asphalt pavement is an environmentally friendly pavement. Due to the rich air voids, the drainage ability, frictional property and sound absorption ability of porous asphalt pavement are higher than those of asphalt concrete (AC) pavement. The void structure of the road surface can effectively reduce noise, which spreads from the interface of the road and the tire. Thus, it is significant to study the air void structure of porous asphalt concrete (PAC) [5].

During engineering, it is inconvenient to obtain the air void structure in PAC; therefore, most existing studies have focused on the effects of macroscopic indicators on the noise

reduction capability of PAC. Dai and Lou [6] conducted near-field noise measurements on asphalt concrete pavement with a nominal maximum particle size of 13 mm (AC-13) and porous asphalt concrete pavements with a nominal maximum particle size of 13 mm (PAC-13), ascertaining the sound-decreasing level. Luong et al. [7] analyzed the influences of different contents of rubber additives on the sound absorption coefficient (SAC) of AC-13, whose results showed a positive relationship. By analyzing the mix grading, component percentage, aggregate shape, and other factors, Losa and Leandri [8] predicted the SAC of PAC-13 using the Neithalath model. Tang [9] verified that a double-layer porous asphalt pavement structure still has a high noise reduction performance under semirigid subgrade conditions. Although the test results of noise value could be used to compare the effect of reducing sound between PAC pavement and AC pavement, the noise absorption mechanism of PAC is difficult to be found by the macroscopic evaluation of noise reduction value.

The sound absorption capability of PAC is highly affected by the size and morphology of voids. Accordingly, it is important to accurately obtain the void structure, which supports further research on the noise reduction effect of PAC. Industrial computed tomographic (CT) scanning is the primary technology used to acquire a microscopic view of PAC structures with voids. Masad et al. [10] used a mathematical method of multiple regression to predict the air void distribution in PAC and estimate the water permeability by void morphology, which shows adequate accuracy. Pei et al. [11] investigated the fractional dimension of voids and void content, revealing a positive correlation between them. Jiang et al. [12] introduced image processing techniques to investigate the relationship between the macroscopic performance of PAC and microscopic features, which revealed that they were closely related. Gao et al. [13] imposed CT scanning images to determine the true depth of structural voids to adjust the sand spreading method for PAC. Wang et al. [14] adopted a 3D reconstruction technique to obtain void parameters, including void surface area, void volume and equivalent void diameter, by which a prediction model for SAC, which possesses high simulation accuracy, was created. Sun et al. [15–18] employed finite element software to examine the sound transmission loss (STL) of cross-sectional images; the result was very similar to the test values, demonstrating the correctness of the simulation. Some research established the simplified void models using acoustic-electric analogy theory or Helmholtz resonance theory [19,20], but it is essential to acquire the material's properties and void characteristics, which were difficult to obtain. The mentioned researches focus mainly on the void characteristic, but the effect of the void on sound absorption has been less concerned, which is the key to revealing the noise reduction mechanism of PAC.

In conclusion, previous research studies have provided most of the macroscopic indicators for the noise reduction design of PAC, and the relationship between void parameters and noise reduction impact has been investigated from a microscopic perspective. However, how to reveal the noise reduction mechanism of PAC with voids is still a challenge to be addressed. This research is aimed at solving the above problems. Two highlight points were proposed: one is the statistical models between void parameters of PAC and SAC and the other is the FEM established by CT images, which shows high accuracy in SAC prediction. Both two highlights are helpful to the further study of the sound absorption capability of PAC and useful to the practical design of low-noise pavement.

In this paper, the relationship between the air voids and the sound absorption capability of PAC was examined. First, the transfer function method was used to obtain the SAC spectrum of PAC with different void contents. Second, the void structure, identified from CT scanning images, was used to analyze the microscopic parameters. Third, statistical models between microscopic parameters and SAC were established. Last, a finite element model based on CT section images was built to predict the SAC spectrum of PAC and explore the noise reduction mechanism of porous asphalt pavement at the microscopic scale.

2. Samples Preparation

2.1. Materials

The technical indexes of the aggregates are shown in Table 1. To model high-quality PAC samples, styrene butadiene styrene (SBS)-modified asphalt combined with a high-viscosity asphalt (HVA) modifier at a ratio of 92:8 (asphalt:modifier) was used in this study. Tables 2 and 3 show the results of the HVA, SBS-modified asphalt and composite-modified asphalt (both SBS and HVA were used to modify the asphalt) technical indicator tests. The technical indexes of the materials meet the requirement of Chinese standards [21,22].

Table 1. Technical indexes of the aggregate.

Sieve Size (mm)	Technical Indexes	Test Results	Normative Requirements	Test Method
10–15	Relative density of the bulk volume	2.81	-	T 0304-2005
	Apparent relative density	2.89	≥2.6	-
	Ruggedness (%)	0.9	≤12	T 0314-2000
	Water absorption rate (%)	1.2	≤2	-
	Needle sheet content (%)	6.9	≤1	T 0312-2005
	Los Angeles wear value (%)	9.3	≤20	T 0317-2005
	Adhesion of the coarse aggregate to asphalt (Level)	5	≥5	T 0616-1993
5–10	Relative density of the bulk volume	2.80	-	T 0304-2005
	Apparent relative density	2.88	≥2.6	-
	Ruggedness (%)	0.9	≤12	T 0314-2000
	Water absorption rate (%)	1.3	≤2	-
	Needle sheet content (%)	8.3	≤1	T 0312-2005
	Los Angeles wear value (%)	9.3	≤20	T 0317-2005
	Adhesion of the coarse aggregate to asphalt (Level)	5	≥5	T 0616-1993
0–5	Apparent density (g/cm^3)	2.738	≥2.60	T 0328-2005
	Methylene blue number (g/kg)	0.9	≤1.5	T 0349-2005

Table 2. Technical indexes of the HVA high-viscosity modifier.

Technical Indexes	Test Results	Normative Requirements	Test Method
Appearance	Uniform and full particles	Uniform and full particles	T860.2-2013
Density (g/cm^3)	0.981	0.90~1.00	T860.2-2013
Single particle mass (g)	0.022	≤0.03	T860.2-2013

Table 3. Technical indexes of the modified asphalt.

Technical Indexes	SBS Modified Asphalt	Normative Requirements	Composite Modified Asphalt	Normative Requirements	Test Method
Density (g/cm^3)	1.035	-	1.029	-	T 0603-2011
Needle penetration (0.1 mm)	55.0	≥50	45	≥40	T 0604-2011
Softening point (°C)	27.2	≥20	35	≥30	T 0605-2011
Ductility (5 °C) (cm)	87.0	≥75	98.0	≥90	T 0606-2011
60 °C Dynamic viscosity (Pa·s)	1576	≥800	439,819	≥400,000	T 0620-2000

2.2. Aggregate Gradation

The passage rates of the 2.36 mm sieve ($P_{2.36}$) and 4.75 mm sieve ($P_{4.75}$) have a significant impact on the void content of PAC-13 [23]. The $P_{2.36}$ and $P_{4.75}$ are closely related to the maximum theoretical relative density by which the void content is affected. Therefore, four PAC-13 gradations with target void contents of 16%, 18%, 22% and 24% were designed by altering $P_{2.36}$ and $P_{4.75}$, which were numbered A1, A2, A3 and A4, respectively. The gradations and the void content of samples (A1~A4) are shown in Table 4; the asphalt–stone ratio was calculated by using the leak test and the Cantabro test.

Table 4. Aggregate gradation of PAC.

Sieve Size (mm)	Passing Percent (%)			
	A1	A2	A3	A4
19.0	-	-	-	-
16.0	100	100	100	100
13.2	95	95	92.7	95
9.5	71	68	56.8	40
4.75	30	28.5	16.7	10
2.36	20	20	10.4	9
1.18	14.7	14	7.9	7
0.60	10.6	9	6.6	6
0.30	9.2	8.5	5.2	5
0.15	7.5	7	4.5	4
0.075	6	4	3.8	3
Asphalt–stone ratio (%)	4.78	4.81	3.70	3.67
Target void content (%)	16.0	18.0	22.0	24.0
Tested void content (%)	16.29	18.51	20.78	23.59

2.3. Test Scheme

The main raw materials of PAC models include aggregate and asphalt. In this test, basalt, basalt machine-made sand and limestone powder were used as the coarse aggregate, fine aggregate and mineral powder filler, respectively. The aggregate was sieved using a sieve shaker. After the cleaning and drying, the aggregate was set in a heating cabinet at 160 °C for 90 min. The SBS-modified asphalt was heated to a liquid state before the models were made. At the beginning of the test, the aggregate was poured into the concrete mixing machine singly. After 60 s, the weighed HVA modifier was put into the machine and stirred together with the aggregate. After 30 s, the quantitative SBS-modified asphalt was finally poured. After 90 s, the PAC was completed. At last, the concrete was taken from the machine to fill the rutting plate mold which was heated to 165 °C. The heating and mixing schemes were carried out above 160 °C.

To verify the basic performance of the PAC, the Marshall test pieces were made by the aggregate gradation of the A4 sample. The main tested results of Marshall stability, dynamic stability, fly-away loss and Marshall flow are 6.97 kN, 9719 times/mm, 14.1% and 27.8 mm. All the technical indexes of the Marshall sample satisfy the requirements of Chinese specifications [22].

The dimensions of all the rutting plate models were 300 mm × 300 mm × 40 mm. Each model was cut into 9 cuboids with the same size of 100 mm × 100 mm × 40 mm. The sample at the center of the rutting plate models after cutting was chosen as the study sample for further investigation in this study. The samples were also named A1~A4, the same as the corresponding gradation in Table 4.

3. Porous Asphalt Concrete Macroscopic Sound Absorption Properties

3.1. Sound Absorption Coefficient Test

The SAC is frequently regarded as the sound absorption performance evaluation parameter. By using the transfer function method [24], the SAC spectra of samples A1~A4 were measured at different frequencies. Figure 1 shows the instrument for the SAC measurements.

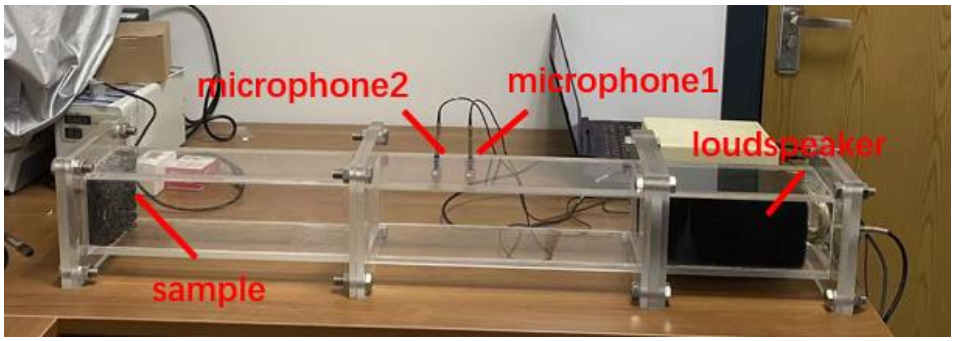

Figure 1. SAC measuring device.

3.2. Result Analysis

Although the traffic noise spectrum has an extremely wide frequency distribution range (20 Hz to 20,000 Hz), the frequency band from 500 Hz to 1500 Hz is the noise frequency range of traffic noise energy [25]. As a result, the sound absorption performance of samples in the frequency range of 500–1500 Hz was investigated in this study. Figure 2 and Table 4 show the analysis results of the SAC test.

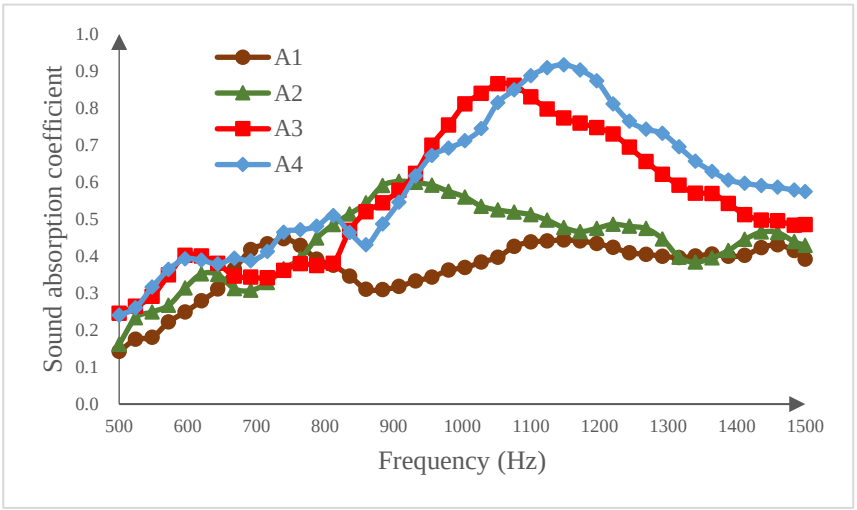

Figure 2. Sound absorption coefficient spectrum.

The SAC results of samples A1~A4 are shown in Figure 2 and Table 5. The peak absorption coefficients of A1~A4 are 0.45, 0.59, 0.88 and 0.93, which are found at 725 Hz, 910 Hz, 1050 Hz and 1140 Hz, respectively. In most frequency ranges, the SAC of samples A3 and A4 exceeded 0.5, resulting in good noise reduction effects. It can be concluded that the SAC of PAC gradually increases with increasing frequency, reaches a peak, and then decreases as the frequency increases. The peak SAC corresponds to the frequency band mostly located in the range of 700 to 1200 Hz. According to research on the dominant traffic noise frequency, PAC can effectively reduce noise caused by small cars. As the void content increases, the band of the SAC spectrum widens, the peak and mean values of SAC increase and the frequency corresponding to the peak increases, which causes the overall spectrum curves to show a trend of moving up and to the right. This means that the overall noise reduction effect improves.

Table 5. Statistical results of the sound absorption coefficient α.

Sample Number	Void Content (%)	Peak α	Peak Corresponding Frequency (Hz)	Mean α
A1	16.29	0.45	725	0.39
A2	18.51	0.59	910	0.42
A3	20.78	0.88	1050	0.55
A4	23.59	0.93	1140	0.59

4. Study of the Microscopic Void Characteristics of PAC

4.1. Computed Tomography Image Segmentation

The characteristics of voids are critical for understanding the PAC noise reduction mechanism. In this study, the CT images of four samples were obtained using industrial CT scanning technology. The CT scanning equipment was set parallel to the height of the samples, as shown in Figure 3. The scan spacing was set to 0.80 mm in the vertical X and vertical Y directions and the images were obtained after rejecting the ends. Figure 4a shows a CT image of sample A2.

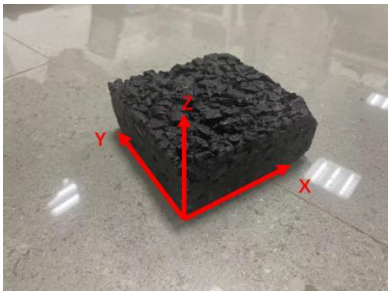

Figure 3. This is a figure. Schemes follow the same formatting.

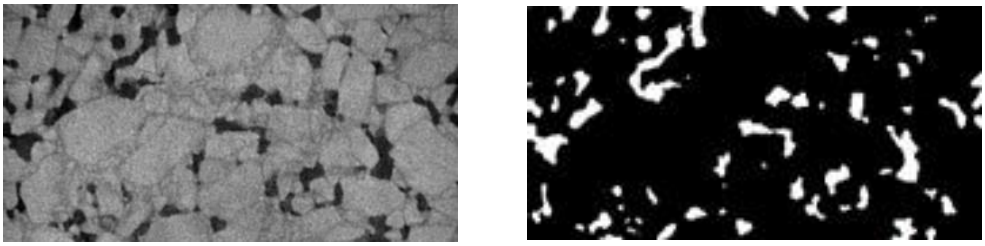

(**a**) (**b**)

Figure 4. CT image segmentation: (**a**) Original CT scan image; (**b**) Identified void structure.

The Otsu method is a simple and efficient image binarization algorithm without losing precision [26]. This method was utilized to segment the CT images and identify void structures in the images. Using the CT image in Figure 4a as an example, the processing result is displayed in Figure 4b, demonstrating that the concrete and voids can be correctly and fully separated. Among all the analysis results of the CT images, the aggregates were not misdiagnosed as voids. Therefore, the quality of this void identification can satisfy the requirements of this investigation.

4.2. Void Characteristics Analysis

The CT images were processed to identify the void structures in the samples [27–30]. In this paper, the analysis of void characteristics was conducted using CT images that are vertical to the X-axis and the Y-axis. The characteristic parameters of the void were identified by writing programs in MATLAB, including N as the average number of voids

within each image, a as the average area of individual voids and d as the equivalent diameter of voids. The calculations are as follows:

$$N = \frac{\sum_{i=1}^{n} N_i}{n} \tag{1}$$

$$A = \frac{\sum_{i=1}^{n} A_i}{n} \tag{2}$$

$$a = \frac{A}{N} \tag{3}$$

$$d = \frac{a}{l} \tag{4}$$

where N_i is the total number of voids in the sample's i-th layer cross-sectional image; n is the total number of layers in the CT scan; A_i is the total area of voids in the sample's ith layer cross-sectional image; A is the average area of voids in all cross-sectional pictures of each sample and l is the average length of each void.

To compute the void content of CT scan identification, the total area of voids within each cross-sectional picture was transformed into the void content of each layer, and the average value was determined.

The aforementioned formulas only describe the size and number of voids, not their morphological properties. Because the internal voids of PAC have obvious fractal properties [31], in this paper, the fractal dimension was used to evaluate the internal complexity of voids, with the box-counting method in fractal theory as the quantification criterion. The CT images were divided by a square grid with a side length δ; the number of boxes $N(\delta)$ occupied by the image boundary with the corresponding side length δ was counted separately. The side lengths of the square grid were then changed, which generates different side lengths with corresponding grid numbers. The side lengths δ and the grid numbers $N(\delta)$ were linearly regressed in logarithmic coordinates, with the slope D of the regression line representing the fractal dimension measured using the box-counting method. The formulations are as follows:

$$N(\delta) = k\delta^{-D} \tag{5}$$

taking the logarithm of both sides of Equation (14) simultaneously, that is, Equation (15).

$$lgN(\delta) = lgk - Dlg\delta \tag{6}$$

$$D_B = \frac{\sum_{i=1}^{n} D_i}{n} \tag{7}$$

where D_i is the fractal dimension within the i-th layer of the section images of the sample and D_B is the average fractal dimension within all section images of the sample.

Table 6 shows the microscopic void characteristics of samples A1~A4. The void content obtained by image recognition technology is very similar to the void content measured by the volume method. The recognition void content is slightly smaller than that obtained by actual measurement, which is due to the limitations of CT scanning accuracy and algorithm recognition accuracy. There are micro-voids that are difficult to identify, which results in a smaller identification void content.

Table 6. Void characteristics of PAC.

Sample Number	Void content (%)		N	d (mm)	D_B
	Test	Identification			
A1	16.29	16.17	49.1	4.1	1.237
A2	18.51	17.97	43.9	4.9	1.251
A3	20.78	20.71	42.0	5.2	1.267
A4	23.51	23.13	37.6	5.8	1.304

For samples A1~A4, Figure 5 shows the relationship between the void content determined and the void structural parameters, including the equivalent diameter and the average number of voids within each image. The measured void content is represented by the horizontal coordinate x, while the double vertical coordinates y_1 and y_2 represent the void equivalent diameter and the average number of voids within each image, respectively. For y_1 and y_2, linear fits are performed and the resulting relational equation and correlation coefficient R^2 are shown in Figure 5. The number of voids inside the PAC decreases as the void content increases but the void equivalent diameter continuously increases, which reveals that the void content of PAC increases not because the number of voids increases but because the void size increases.

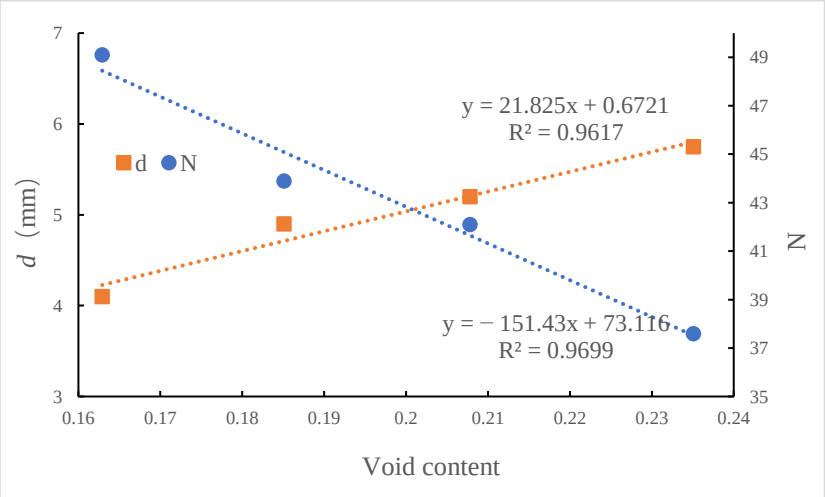

Figure 5. Relationship between d, N and the void content.

The relationships between the above parameters and the peak and mean values of the SAC (named α in the figures) of the PAC are shown in Figure 6a,b. The results follow the same pattern as the improvement in noise reduction performance caused by increasing the macroscopic void content. Although an increase in void content reduces the number of voids, the fitted results show that the sensitivity of the SAC with the equivalent diameter is greater than that of the number of voids. This indicates that while the number of voids decreases, the equivalent diameter demonstrates a greater increase in the noise reduction effect, which proves that an increase in void diameter can increase the incident acoustic waves and provide a larger internal surface area for sound energy reflection and frictional attenuation. When the two void parameters change, the peak value of the SAC changes more than the mean value. It can be seen that as long as the PAC's design void content requirements (16–25%) are met, PAC may provide good noise reduction in most frequency bands.

The geometric complexity of the void structure is described by the fractal dimension. Figure 7 shows the relationship between the void content and the average fractal dimension of all images of each sample. As the void content increases, D_B increases, showing that as the complexity of the void morphology improves, the structure of the internal voids of the PAC becomes more complicated and the internal roughness rises.

As shown in Figure 8, the noise reduction impact improves as the fractal dimension grows, which results from a more complicated void structure, leading to a greater chance of acoustic wave reflections when the waves enter the interior void structure. Due to the increase in the fractal dimension, the interface between the acoustic waves and the void surface is increased, providing a larger friction area. This causes greater viscous loss generated between the air and the void wall, resulting in a higher SAC.

The fractal dimension of the voids can explain the variation in SAC with d and N. As the void content increases, N decreases, which seems to reduce the space where sound energy is lost. However, the increase in d increases the sound wave incidence and D_B

increases with increasing void content, which enhances the amount of sound energy loss inside the structure; the overall sound absorption and noise reduction performance of the structure is improved.

The three characteristics, d, N and D_B, are strongly correlated with the SAC. These characteristics may be used to design PAC pavement sound absorption performance in the future.

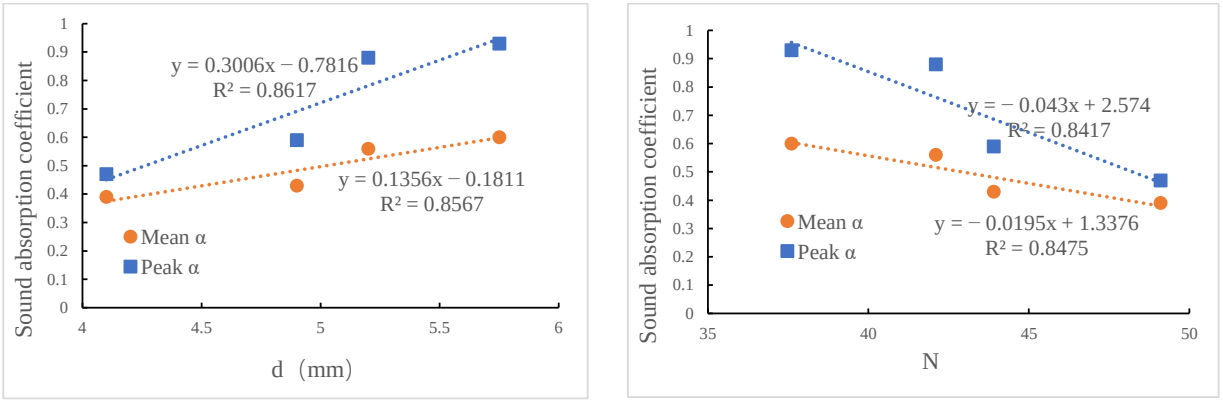

(**a**) (**b**)

Figure 6. The relationship between the SAC and the parameters of size and number: (**a**) Relationship between SAC and N; (**b**) Relationship between SAC and d.

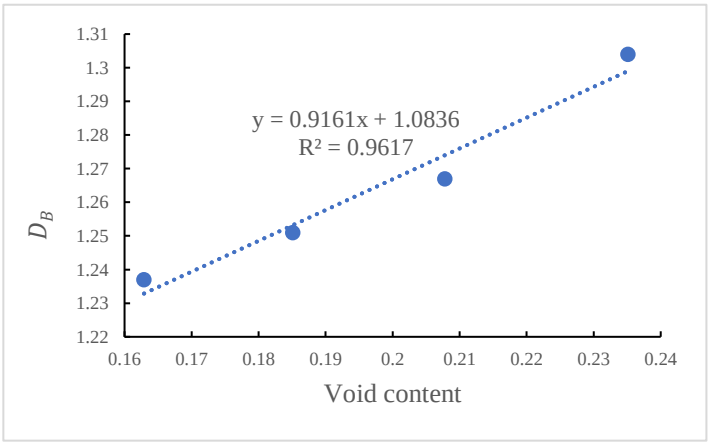

Figure 7. Relationship between D_B and the void content.

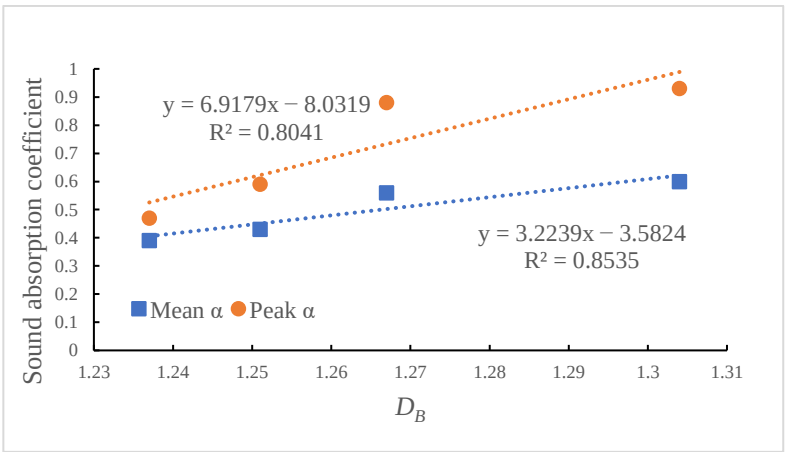

Figure 8. Relationship between the SAC and D_B.

5. Finite Element Simulation of Void Structure

5.1. Theory of Finite Element Models

The internal interconnected voids of PAC and the damping of the material itself perform the functions of sound absorption and noise reduction. As a result, not only must the continuity equation for fluid momentum conservation (named the Navier–Stokes equation, N-S equation) be considered in this problem but also the structural dynamics equations. The following equations are available for a compressible Newtonian fluid [32]:

$$\rho\left(\frac{\partial v}{\partial t} + v{\cdot}\nabla v\right) = -\nabla p + \nabla{\cdot}\left(\mu\left(\nabla v + (\nabla v)^T\right) - \frac{2}{3}\mu(\nabla{\cdot}v)I\right) + F \tag{8}$$

where v is the speed of sound; p is the sound pressure; ρ is the air density and μ is the aerodynamic viscosity. From left to right, each part of the formula represents the inertial force, acoustic pressure, viscous force and external force.

$$\frac{\partial p}{\partial t} + \nabla{\cdot}(\rho v) = 0 \tag{9}$$

Equations (17) and (18) should be solved simultaneously; they represent momentum conservation and mass conservation, respectively. By solving these two equations under specified boundary conditions, the fluid flow rate and pressure inside a given structure can be obtained. The analytical solution is often difficult to obtain accurately due to the complexity of the equations and the structure itself. As a result, solving the equations necessitates the simplification of the assumed conditions and the structure with the application of numerical methods [33].

When air is assumed to be a non-viscous compressible and homogeneous fluid, the N-S equation can be simplified to Equation (19), which means the acoustic fluctuation equation [34].

$$\frac{1}{v^2}\frac{\partial^2 p}{\partial t^2} - \nabla^2 p = 0 \tag{10}$$

In the finite element method, the discretized sound field fluctuation equations and structural dynamics equations are Equations (11) and (12).

$$\left\{M_e^p\right\}\{\ddot{p}_e\} + \left\{K_e^p\right\}\{p_e\} + \rho_0[R_e]^T\{U\} = 0 \tag{11}$$

$$[M_e]\left\{\ddot{U}_e\right\} + [C_e]\left\{\dot{U}_e\right\} + [K_e]\{U_e\} = \{F_e\} \tag{12}$$

The acoustic pressure term acting at the air-pavement interface is added to the right-hand side of the structural dynamic Equation (12) to couple the fluid to the solid and obtain Equation (13):

$$[M_e]\left\{\ddot{U}_e\right\} + [C_e]\left\{\dot{U}_e\right\} + [K_e]\{U_e\} = \{F_e\} + \left\{F_e^{pr}\right\} \tag{13}$$

We discretize the acoustic pressure vector $\left\{F_e^{pr}\right\}$.

$$\left\{F_e^{pr}\right\} = [R_e]\{p_e\} \tag{14}$$

Then, Equation (13) can be simplified into equation (15).

$$[M_e]\left\{\ddot{U}_e\right\} + [C_e]\left\{\dot{U}_e\right\} + [K_e]\{U_e\} - [R_e]\{p_e\} = \{F_e\} \tag{15}$$

Combining Equation (11) with Equation (15), the acoustic-solid coupling Equation (16) can be obtained as follows:

$$\begin{bmatrix} [M_e] & [0] \\ \left[M^{fs}\right] & \left[M_e^p\right] \end{bmatrix} \begin{Bmatrix} \{\ddot{U}_e\} \\ \{\ddot{p}_e\} \end{Bmatrix} + \begin{bmatrix} [C_e] & 0 \\ 0 & 0 \end{bmatrix} \begin{Bmatrix} \{\dot{U}_e\} \\ \dot{p}_e \end{Bmatrix} + \begin{bmatrix} [K_e] & \left[K^{fs}\right] \\ 0 & \left[K_e^p\right] \end{bmatrix} \begin{Bmatrix} \{U_e\} \\ \{p_e\} \end{Bmatrix} = \begin{Bmatrix} \{F_e\} \\ 0 \end{Bmatrix} \tag{16}$$

where $\left[M^{fs}\right] = \rho_0 [R_e]^T$ is the mass coupling matrix; $\left[K^{fs}\right] = -[R_e]$ is the stiffness coupling matrix; $\left[M_e^p\right]$ is the fluid mass matrix; $\left\{K_e^p\right\}$ is the fluid stiffness matrix; $[M_e]$ is the mass matrix of the solid structure; $[C_e]$ is the damping matrix of the solid structure; $[K_e]$ is the stiffness matrix of the solid structure; $\{U_e\}$ is the solid displacement matrix; $\{p_e\}$ is the fluid displacement matrix and $\{F_e\}$ is the exogenic force.

5.2. Construction of the Finite Element Model

Sound absorption in porous asphalt pavements is a common acoustic-solid coupling problem that is influenced by a variety of factors, such as air temperature, humidity and vehicle loading, in real-world situations. The majority of existing research has focused on the fields of pressure acoustics or fluctuating acoustics using air as the analysis medium [35–37]. The damping of pavement structures also has an impact on sound absorption. The sound pressure acts on the structure, causing structural vibrations. At the same time, the structural vibrations cause the surrounding air to vibrate, causing sound waves to radiate outward. The mass coupling matrix and the stiffness coupling matrix are used in Equation (16) to represent this pair of interactions.

Numerical solutions were obtained by using the finite element method in this paper. COMSOL Multiphysics is a finite element simulation program that can handle a coupled multi-physics field. This software was used in this study to couple pressure acoustics and solid mechanics to obtain an acoustic-structural boundary. In the simulated results, including the calculated sound pressure and sound pressure level distribution, the noise reduction effect of PAC was analyzed under different void contents, which explains the noise reduction mechanism of PAC from a microscopic perspective.

The void structure of PAC is complicated and the distribution of void locations is extremely random. To obtain an accurate void structure, the processed CT images of the PAC samples were used as the import model. For each sample, as the image processing and void identification operations described in Chapter 3.1, the bitmap images were obtained. The bitmap images in this paper were programmed to be converted into vector images in AutoCAD format, which were used as the import models by the COMSOL CAD interface. The result is shown in Figure 9.

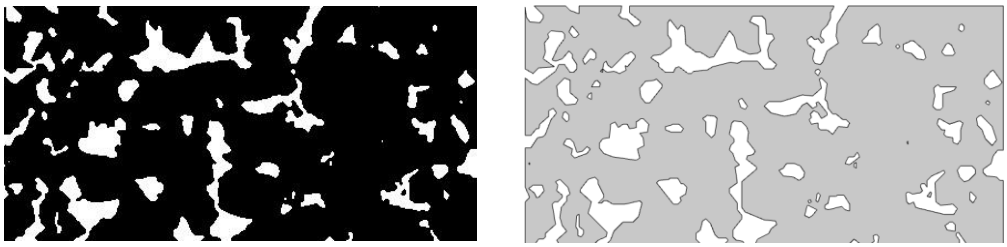

(**a**) (**b**)

Figure 9. Image import: (**a**) Cross-sectional view; (**b**) Model establishment.

The media involved in the simulation are air and PAC. Based on existing studies [38–40], the required material parameters are summarized, as shown in Table 7.

Because material parameters change with external temperature, humidity and other factors, the following assumptions were made to clarify the study's scope and accurately describe the noise absorption of PAC.

1. The acoustic calculations in this paper are solved under linear acoustic conditions. The acoustic pressure is very small compared to the atmospheric pressure because it

is the residual pressure after the atmospheric pressure perturbation. Therefore, in this paper, a compressional wave under a small acoustic perturbation is considered.

2. All the air particles conduct simple harmonic vibration at the acoustic equilibrium position. In this paper, it is assumed that no air flow occurs in the air flow field, i.e., no wind condition. Therefore, the N-S equation can be simplified to a linear N-S equation.
3. The void wall surface is completely filled with air. In the model, the air is in continuous and complete contact with the void structure.
4. The adiabatic condition is applied to the air model boundary. The thermal energy generated by friction between the air and the void wall raises the temperature of the PAC but it does not exchange heat with the air. Only the sound absorption effect at 293.15 K is taken into account.
5. The incident direction of the sound source is selected as the Z direction. The type and size of the sound source have no effect on the final calculation results because the material's SAC is its own property. In this paper, the incident source is a plane wave perpendicular to the surface of the sample model with a pressure amplitude of 1 Pa.

Table 7. Material parameters involved in the simulation.

Materials	Density (kg/m^3)	Modulus (MPa)	Poisson's Ratio	Thermal Conductivity (W/(m·K))	Specific Heat Capacity (kJ/(kg·K))	Coefficient of Thermal Expansion (1/K)	Sound Velocity (m/s)
Air	1.205	0.142	-	0.0257	1.005	3.43×10^{-3}	343
PAC-13	2039	2900	0.3	0.8705	1200	1.60×10^{-5}	3500

The model of the measuring instrument was established and the transfer function method was used to obtain the SAC, in which the sizes of the instrument, the position and the spacing of the microphone were designed according to the actual instrument to visualize the difference between the simulation model and the measured sound absorption effect. The model is shown in Figure 10.

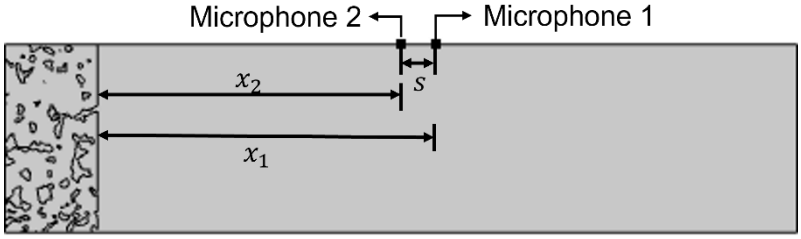

Figure 10. Model of the impedance tube. x_1: the distance of microphone 1 from the reference surface, x_2: the distance of microphone 2 from the reference surface.

The working principle is that the two microphones measure the incident and reflected sound pressures, which are used to calculate the transfer function. The SAC is calculated from the incident sound reflection factor determined by the transfer function. The calculation process is shown as follows.

If the side of the sample in contact with the acoustic wave is the reference surface ($x = 0$), then the distance of microphone 1 from the reference surface is x_1 and the distance of microphone 2 from the reference surface is x_2, as the Figure. 10 shown. The incident sound pressure p_i and the reflected sound pressure p_R can be expressed as:

$$p_i = \hat{p_i} e^{jk_0 x} \tag{17}$$

$$p_R = \hat{p_R} e^{-jk_0 x} \tag{18}$$

where $\hat{p_i}$ is the amplitude of P_i on the reference plane; $\hat{p_R}$ is the amplitude of P_R on the reference plane; $k_0 = k_0^{'} - jk_0^{''}$ is the complex wavenumber.

The sound pressures p_1 and p_2 at the two microphone positions are:

$$p_1 = \hat{p}_i e^{jk_0 x_1} + \hat{p_R} e^{-jk_0 x_1} \tag{19}$$

$$p_2 = \hat{p}_i e^{jk_0 x_2} + \hat{p_R} e^{-jk_0 x_2} \tag{20}$$

If the distance between microphones 1 and 2 is $x_1 - x_2 = s$, then the incident and reflected wave transfer functions H_1 and H_R are:

$$H_1 = \frac{p_{21}}{p_{11}} = e^{-jk_0 s} \tag{21}$$

$$H_R = \frac{p_{2R}}{p_{1R}} = e^{jk_0 s} \tag{22}$$

If the incident acoustic reflection factor is r, then $\hat{p_R} = r\hat{p}_i$, and the total sound field transfer function H_{12} can be derived by combining Equations (19) and (20) as follows:

$$H_{12} = \frac{p_2}{p_1} = \frac{e^{jk_0 x_2} + re^{-jk_0 x_2}}{e^{jk_0 x_1} + re^{-jk_0 x_1}} \tag{23}$$

Combining Equation (21) with Equation (22), we can obtain r as Equation (24):

$$r = \frac{H_{12} - H_1}{H_R - H_{12}} e^{2jk_0 x_1} \tag{24}$$

Therefore, the SAC α can be calculated by r, as shown in Equation (25):

$$\alpha = 1 - \left| r^2 \right| = 1 - r_r^2 - r_i^2 \tag{25}$$

where r_r is the real part of the incident acoustic reflection factor and r_i is the imaginary part of the incident acoustic reflection factor.

The pressure acoustic module and the structural mechanics module were added to the model after it was established; the acoustic-solid coupling interface for both is generated by the COMSOL automatically, after which the mesh can be divided. Notably, if the size of the divided cells is too large, then the final model calculation results will be distorted and will have difficulty converging [24]. An acoustic medium cell was used in this study, whose size is smaller than 1/6 of the wavelength corresponding to the calculated maximum frequency (1500 Hz). Figure 11 shows the grid created by dividing the imported CT image in Figure 9, in which the blue part represents the air and the gray part represents the PAC model.

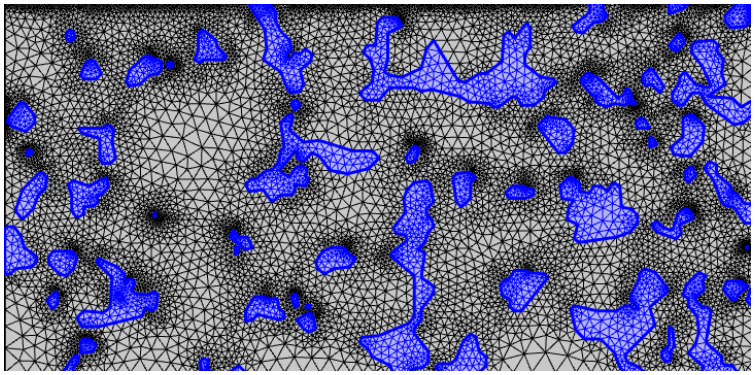

Figure 11. Model after meshing.

5.3. Analysis of the Simulation Results

In this analysis, the model was swept in steps of 25 Hz in the frequency range of 500–1500 Hz after meshing was completed. As calculated from parts of CT images of

A1~A4, Figure 12 shows the distribution of the sound pressure levels for four different void content PAC structures at different frequencies.

Figure 12 shows that PAC-13 has a good sound absorption effect and the sound pressure level has a good grading level. The sound absorption performance of PAC first increases and then decreases with increasing frequency, which is consistent with the results of the macroscopic tests. In the light of the perforated plate principle [31] and the Helmholtz resonator principle [32], the void structures can be regarded as sound absorbers. When the frequency is close to the resonant frequency, the SAC of PAC is larger than the frequency deviating from the resonant frequency. Because the noise-reducing capability of small voids is limited, noise reduction is primarily provided by the large voids. When the void content of PAC increases, the average internal void size and void depth of PAC increase, which improves the sound absorption effect of the whole structure by increasing the space of acoustic vibration. Due to the larger distribution range of void size, there is an obvious noise reduction effect in the middle and high frequency bands.

Figure 12 shows that the voids connecting the surface and the surrounding concrete have superior sound absorption levels and sound waves are more likely to be reflected when transmission occurs in concrete near the interior closed voids. The surface-connected voids are the key structures that provide the PAC noise reduction effect, as seen by these figures. The capacity of PAC to reduce noise is also influenced by the internal complexity of the voids. The void morphology grows increasingly complex as the void content increases, enhancing the overall sound absorption capability. However, the complexity of voids is constrained by their pore size and length. With a small void content, the void structure has a large fractal dimension; however, the small size is more likely to lead to acoustic energy concentration, which is not conducive to energy dissipation. With a large void content, the internal structure of voids being very rough, sound energy can be significantly reduced.

In summary, as the void content rises, the internal voids become more easily joined to create a whole, resulting in noise reduction. The complexity of the void has a favorable effect on the sound absorption performance of PAC. The surface-connected voids are an important structure with respect to the sound absorption performance. However, the void size and the complexity of the voids often affect each other and work together to influence the sound absorption ability of PAC. In a word, as the void size increases, the sound absorption performance of PAC improves.

After importing all models, the COMSOL built-in commands, real (acpr_p) and imag (acpr_p), were used to obtain the real part and the imaginary part sound pressure at the positions of microphones 1 and 2; the SAC was calculated using Equations (1)–(9) and the SAC spectrum of each image was obtained. Each sample can export spectra of 50 images, which were averaged to obtain the simulated SAC spectrum, as shown in Figure 13. The simulation results show the same trend as the measured results, which increase to peak, then consequently decrease. The peak SACs of the simulated A1~A4 samples are 0.42, 0.51, 0.57 and 0.69 at 760 Hz, 975 Hz, 1115 Hz and 1225 Hz, respectively. The structural characteristic frequencies correspond not only to the peak but also to the trough. The overall resonance of the structure at certain frequencies causes a decrease in the absorption coefficient, which is the trough in the spectrum, as shown in Figure 13b,d for the SAC trough at approximately 700 Hz. The simulated results show the same trend as the test values in the 500–1500 Hz range.

In order to analyze the errors between the test and simulation results, maximum errors and average errors were calculated using Equations (26)–(28):

$$\delta_i = \left| \frac{\alpha_1 - \alpha_2}{\alpha_1} \right| \tag{26}$$

$$\overline{\delta} = \frac{\sum_{i=1}^{n} \delta_i}{n} \tag{27}$$

$$\delta_{max} = max\{\delta_i\} \tag{28}$$

where δ_i is the absolute value of the error between test result and simulation result in a single frequency; α_1 is the test SAC of PAC; α_2 is the simulation SAC of PAC; $\overline{\delta}$ is the average error of all frequencies; n is the total number of each frequency, the taken values space is 5 Hz in this paper and δ_{max} is the maximum error at all frequencies.

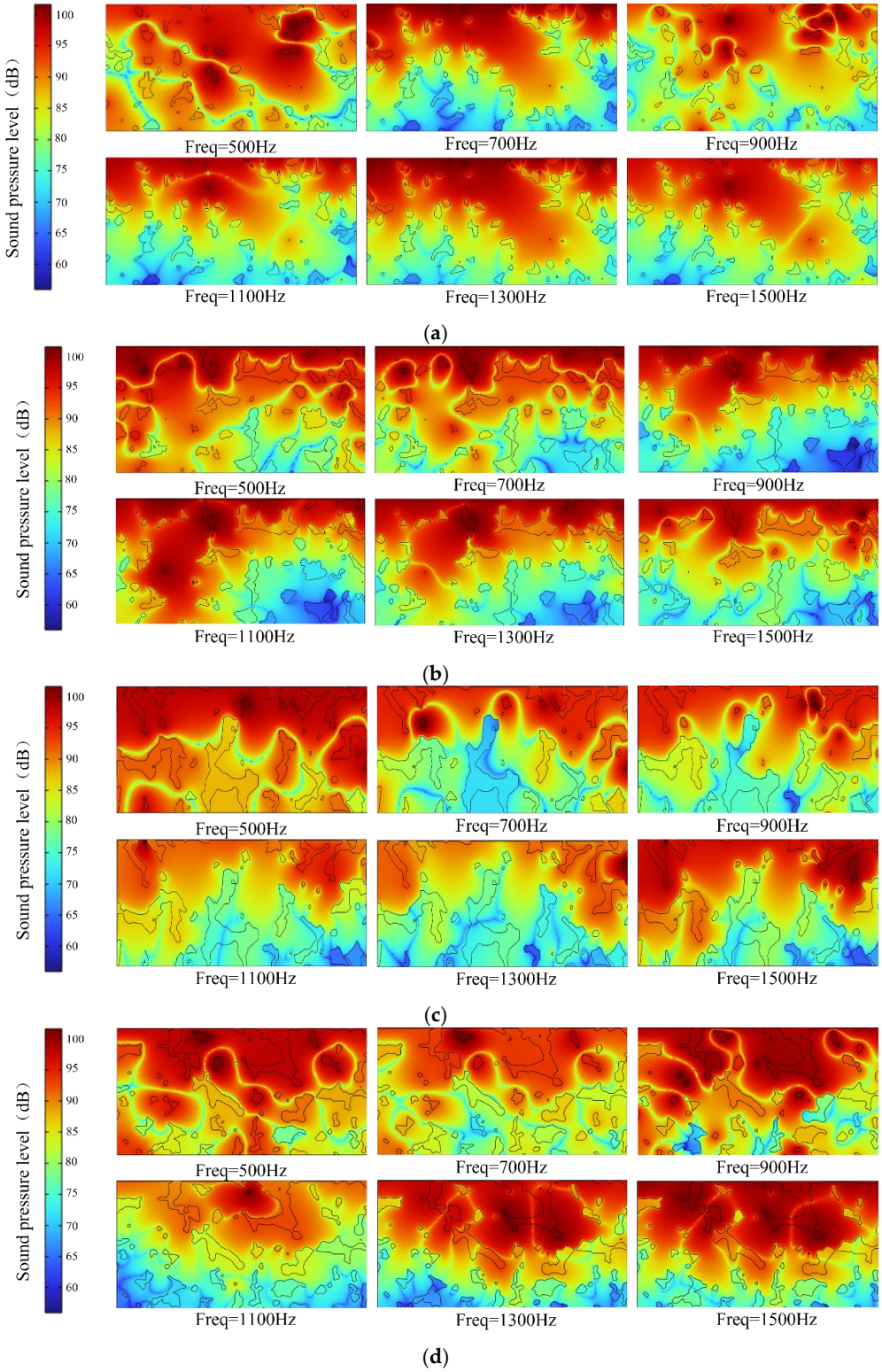

Figure 12. Sound pressure level distribution of PAC with different void contents at different frequencies: (**a**) sample A1; (**b**) sample A2; (**c**) sample A3 and (**d**) sample A4.

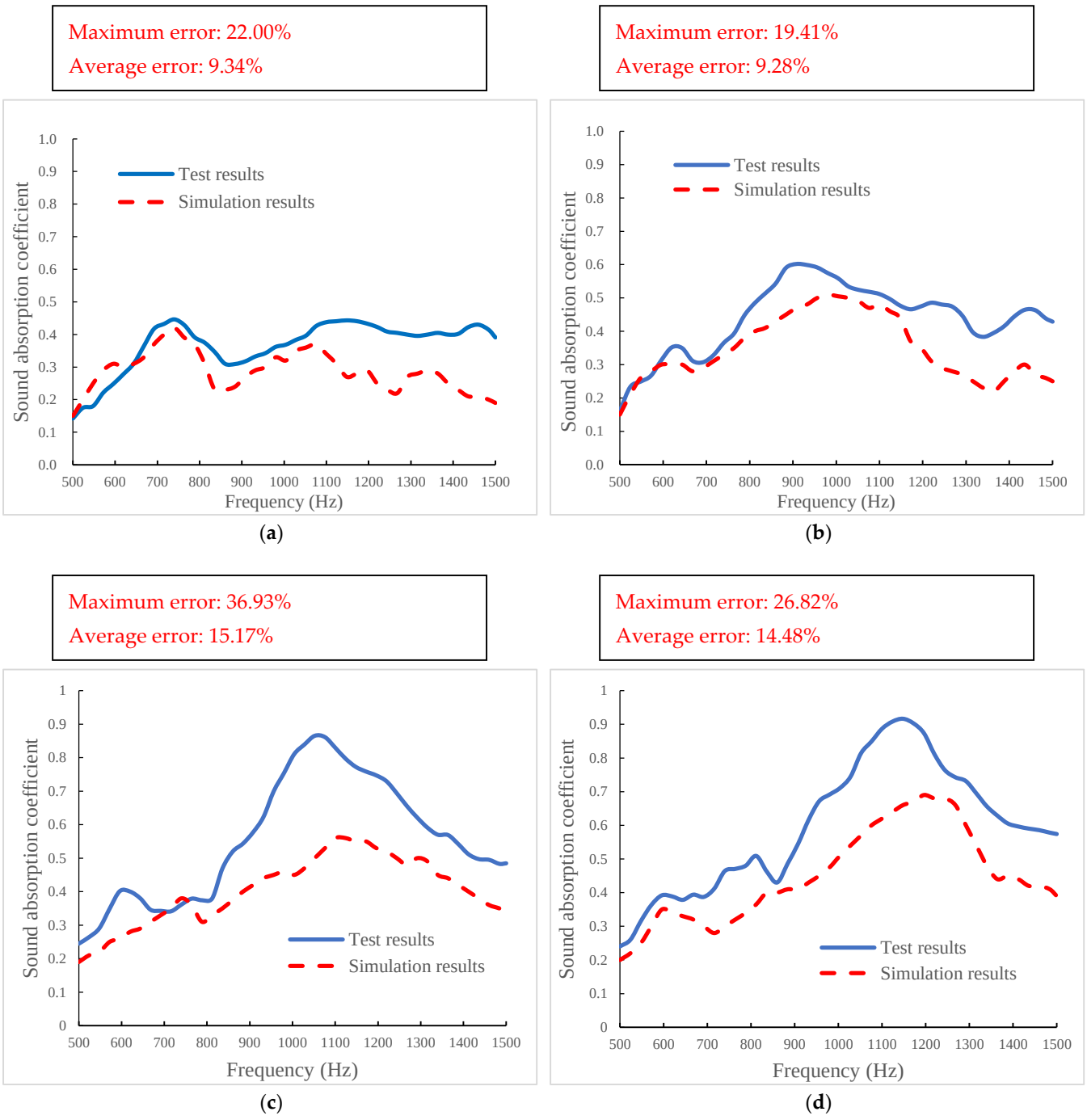

Figure 13. Comparison of SAC spectra between samples A1~A4: (**a**) sample A1; (**b**) sample A2; (**c**) sample A3 and (**d**) sample A4.

The calculated results of errors were listed in Figure 13. The maximum errors of A1~A4 samples are 22.00%, 19.41%, 36.93% and 26.82%. The average errors are 9.34%, 9.28%, 15.17% and 14.48%, respectively. For porous asphalt concrete, the sample with the lower void content has the more accurate simulation result. The average errors of A1 and A2 are both less than 10%. Figure 13 shows the simulation results are more precise at low frequencies (about 500–1000 Hz) and less at high frequencies (1000–1500 Hz). Because the frequencies corresponding to the peak SAC of low void content samples is smaller than the high void content samples, the FEM models are more suitable for PAC with small void content.

Furthermore, the measured results were compared to the mean values of the SAC obtained from the simulations. The measured and simulated SACs of A1 to A4 are shown in Figure 14. Both the tested and simulated results have a strong linear relationship with the void content, with correlation coefficients of 0.9368 and 0.9074, respectively. The simulated values are smaller than the measured values, with the simulated mean values of the absorption coefficients of samples A1 to A4 being 74.36%, 74.47%, 76.77% and 75.01% of the test values, respectively. Combined with Figures 12 and 13, the simulation results are more similar to the experimental results at low frequencies but less so at high frequencies. One reason is that the effect of inner roughness on the loss of acoustic waves grows as the frequency increases. The acquired void structure in this study after the CT scanning, image recognition and vectorization conversion causes the recognition accuracy to be limited, resulting in smaller simulation results than test results at high frequencies. Another reason is that the scanning interval between each cross-sectional image will truncate the surface-connected pores, which are cut into some surface-connected voids and inner voids in each image. The damping qualities of the material and the structure of the voids are primarily responsible for the noise reduction effect of PAC. The material properties can be simulated fully during the simulation process. However, the simulation of voids is limited, which reduces the simulation accuracy. The goal of follow-up research is to determine more about 3D void modeling.

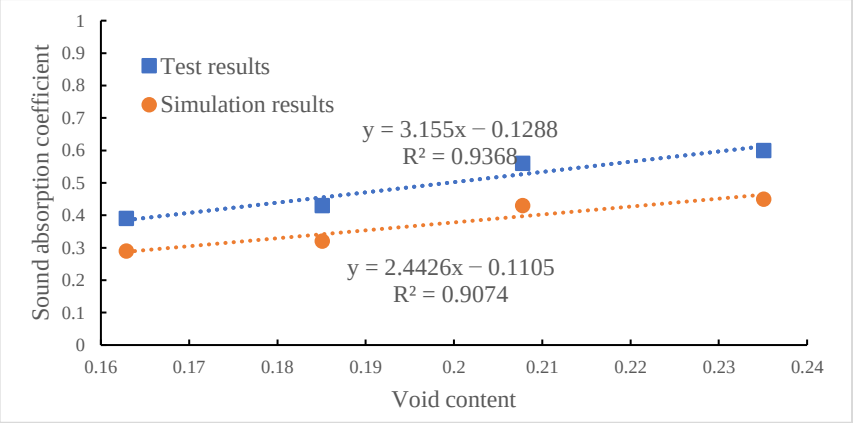

Figure 14. Mean SAC.

The SAC and the structural characteristic frequencies of the test results are similar to those of the simulated results. All the simulated average values of the SAC account for approximately 75% of the measured values. By the comparison between test and simulated results, the reasonableness of the model is proved, which shows that the PAC acoustic model that was created using the CT scanning methodology and the finite element approach is practical.

6. Conclusions

In this paper, CT scanning technology was used to obtain slice images of the PAC samples. Programming was used to identify the voids of the images. The relationship between the characteristic parameters of the voids and the SAC was investigated. The processed CT images were imported into the finite element software to build the acoustic models. Based on the model, the noise reduction mechanism of the void structure was analyzed. The main conclusions are as follows:

1. The SAC spectrum of PAC tends to increase to the peak value and then decrease. As the void content increases, the SAC spectrum curve shows a trend that becomes higher, more rightward and wider, while the peak values and their corresponding frequencies increase. The overall noise reduction effect of PAC is improved;

2. The SAC decreases with an increasing average number of voids and increases with an increasing equivalent diameter of voids and average fractal dimension;
3. The finite element models are built using CT images. At different frequencies, the simulated distribution of the sound pressure level is calculated, which can explain the noise reduction mechanism of PAC;
4. The finite element models can predict the SAC of PAC. At low frequencies, the results are accurate; at high frequencies, the results are smaller than the test results but still acceptable.

Author Contributions: Conceptualization, Data curation, Visualization, Investigation, Writing-review and editing, J.X.; Conceptualization, Formal analysis, Methodology, Writing-original draft, Y.Z.; Investigation, Visualization, Funding acquisition, Z.W. All authors have read and agreed to the published version of the manuscript.

Funding: The Natural Science Foundation of Jiangsu Province (BK20181112).

Institutional Review Board Statement: Not applicable.

Data Availability Statement: Some or all data that support the findings of this study are available from the corresponding author (wangzq911201@nuaa.edu.cn) upon reasonable request.

Acknowledgments: The authors acknowledge the partial support provided by the Natural Science Foundation of Jiangsu Province (BK20181112). Additionally, all the authors of the following references are much appreciated.

Conflicts of Interest: The authors declare no conflict of interest.

References

1. Roswall, N.; Raaschou-Nielsen, O.; Ketzel, M.; Gammelmark, A.; Overvad, K.; Oisen, A.; Sørensen, M. Long-term residential road traffic noise and NO_2 exposure in relation to risk of incident myocardial infarction: A Danish cohort study. *Environ. Res.* **2017**, *156*, 80–86. [CrossRef] [PubMed]
2. *Asphalt Pavement: An International Perspective*; Transportation Research Board: Washington, DC, USA, 1990. Available online: https://binamarga.pu.go.id/bintekjatan/otomasi9/index.php?p=show_detail&id=250&keywords= (accessed on 10 September 2022).
3. Crocker, M.J.; Hanson, D.; Li, Z.; Karjatkar, R.; Vissamraju, K.S. *Measurements of the Acoustical and Mechanical Properties of Porous Road Surfaces and Tire/Road Noise*; Transportation Research Board: Washington, DC, USA, 2004.
4. Woldemariam, W.B.; Dare, T.; Mcdaniel, R.S. *Comparison of Acoustic Absorption Properties of HMA Specimens*; Transportation Research Board: Washington, DC, USA, 2012.
5. Liu, J.W.; Li, H.; Sun, L.J.; Zhang, H.J.; Xie, N.; Tian, Y.; Jia, M.; Fu, K.M.; Yu, B.; Zhu, Y.T. Leachate risks of fine solid wastes in porous asphalt pavement and runoff purification effects of diatomite filler. *J. Clean. Prod.* **2021**, *297*, 126623. [CrossRef]
6. Dai, L.M.; Lou, Z. An Experimental and Numerical Study of Tire/Pavement Noise on Porous and Nonporous Pavements. *J. Environ. Inform.* **2007**, *11*, 62–73. [CrossRef]
7. Luong, J.; Bueno, M.; Vázquez, V.F.; Paje, S.E. Ultrathin porous pavement made with high viscosity asphalt rubber binder: A better acoustic absorption. *Appl. Acoust.* **2014**, *79*, 117–123. [CrossRef]
8. Losa, M.; Leandri, P. A comprehensive model to predict acoustic absorption factor of porous mixes. *Mater. Struct.* **2012**, *45*, 923–940. [CrossRef]
9. Tang, G.Q. Research on Key Technology of Two-Layer Porous and Low-Noise Asphalt Pavement. Ph.D. Thesis, Southeast University, Nanjing, China, 2015.
10. Masad, E.; Jandhyala, V.K.; Dasgupta, N.; Somadevan, N.; Shashidar, N. Characterization of air void distribution in asphalt mixes using x-ray computed tomography. *J. Mater. Civ. Eng.* **2002**, *2*, 122–129. [CrossRef]
11. Pei, J.Z.; Zhang, J.L.; Chang, M.F. Influence of mineral aggregate gradation on air void distribution characteristic of porous asphalt mixture. *China J. Highw. Transp.* **2010**, *23*, 1–6. [CrossRef]
12. Jiang, W.; Sha, A.M.; Xiao, J.J.; Wang, Z.J. Microscopic void features and influence of porous asphalt concrete. *J. Tongji. Univ.* **2015**, *43*, 67–74. [CrossRef]
13. Gao, L.; Liu, M.X.; Wang, Z.Q.; Xie, J.G.; Jia, S.C. Correction of texture depth of porous asphalt pavement based on CT scanning technique. *Constr. Build. Mater.* **2019**, *200*, 514–520. [CrossRef]
14. Gao, L.; Wang, Z.Q.; Xie, J.G.; Wang, Z.X.; Li, H. Study on the sound absorption coefficient model for porous asphalt pavements based on a CT scanning technique. *Constr. Build. Mater.* **2020**, *230*, 117019. [CrossRef]
15. Sun, J.F.; Zhang, H.T.; Wu, G.Y.; Liu, Z.Q.; Feng, Y.P.; Jia, M.H. Micro-structural analysis of noise reduction mechanism of porous asphalt mixture based on FEM. *Multidiscip. Model. Mater. Struct.* **2021**, *17*, 1154–1167. [CrossRef]
16. Sun, J.F.; Zhang, H.T.; Yu, T.J.; Liu, Z.Q. Meso simulation and macro experimental study ofnoise reduction in porous asphalt mixtures. *J. For.* **2021**, *6*, 165–171. [CrossRef]

17. Liu, D.G.; Zhang, H.T.; Yu, T.J.; Sun, J.F.; Shan, Z.H.; He, D.L. Meso-structural characteristics of porous asphalt mixture based on temperature-stress coupling and its influence on aggregate damage. *Constr. Build. Mater.* **2022**, *342*, 128064. [CrossRef]
18. Sun, J.F.; Zhang, H.T.; Yu, T.J.; Wu, G.Y.; Jia, M.H. Influence of void content on noise reduction characteristics of different asphalt mixtures using meso-structural analysis. *Constr. Build. Mater.* **2022**, *325*, 126806. [CrossRef]
19. Praticò, F.G. On the dependence of acoustic performance on pavement characteristics. *Transp. Res. Part D* **2014**, *29*, 79–87. [CrossRef]
20. Chen, D.; Han, S.; Han, X.; Su, Q.; Wang, Z.Y. Acoustic Absorption Model of Porous Asphalt Mixture Based on its Micro Structure. *J. Build. Eng.* **2017**, *20*, 575–581.
21. *JTG E42–2005*; Test Methods of Aggregate for Highway Engineering. Research Institute of Highway Ministry of Transport: Beijing, China, 2005.
22. *JTG E20–2011*; Standard Test Methods of Bitumen and Bituminous Mixtures for Highway Engineering. Research Institute of Highway Ministry of Transport: Beijing, China, 2011.
23. Yu, J.B.; Huang, X.M. Design of equality used in OGFC. *J. Henan Univ. Sci. Tech.* **2004**, *25*, 62–65. [CrossRef]
24. Liu, M.X. Research on Noise Reduction Performance of Porous Asphalt Concrete based on Microstructure. Master's Thesis, Nanjing University of Aeronautics and Astronautics, Nanjing, China, 2020.
25. Qi, L. Evaluation and Optimization on the Sound Absorption of Porous Asphalt Pavement. Ph.D. Thesis, Chang'an University, Xi'An, China, 2011.
26. Otsu, N. A Threshold Selection Method from Gray Level Histograms. IEEE trans. *Intell. Transp. Syst.* **1979**, *9*, 62–66. [CrossRef]
27. Zhao, Y.J.; Wang, X.W.; Jiang, J.W.; Zhou, L. Characterization of interconnectivity, size distribution and uniformity of air voids in porous asphalt concrete using X-ray CT scanning images. *Constr. Build. Mater.* **2019**, *213*, 182–193. [CrossRef]
28. Jiang, J.W.; Zhang, Z.; Dong, Q.; Ni, F.J. Characterization and identification of asphalt mixtures based on Convolutional Neural Network methods using Xray scanning images. *Constr. Build. Mater.* **2018**, *174*, 72–80. [CrossRef]
29. Zhang, K.; Zhang, Z.Q.; Luo, Y.F.; Huang, S.Y. Accurate detection and evaluation method for aggregate distribution uniformity of asphalt pavement. *Constr. Build. Mater.* **2017**, *152*, 715–730. [CrossRef]
30. Yang, B.; Li, H.; Zhang, H.J.; Xie, N.; Zhou, H.N. Laboratorial investigation on effects of microscopic void characteristics on properties of porous asphalt mixture. *Constr. Build. Mater.* **2019**, *213*, 434–446. [CrossRef]
31. Chaudhuri, B.B.; Sarkar, N. Texture segmentation using fractal dimension. *IEEE Trans. Pattern Anal. Mach. Intell.* **1995**, *17*, 72–77. [CrossRef]
32. Ding, Y.M.; Wang, H. FEM-BEM analysis of tyre-pavement noise onporous asphalt surfaces with different textures. *Int. J. Pavement Eng.* **2019**, *20*, 1090–1097. [CrossRef]
33. Wang, H.; Ding, Y.M.; Liao, G.Y.; Ai, C.F. Modeling and optimization of acoustic absorption for porous asphalt concrete. *J. Eng. Mech.* **2016**, *142*, 04016002. [CrossRef]
34. Watts, G.R.; Chandler-Wilde, S.N.; Morgan, P.A. The combined effects of porous asphalt surfacing and barriers on traffic noise. *Appl. Acoust.* **1999**, *58*, 351–377. [CrossRef]
35. Chu, L.; Fwa, T.F.; Tan, K.H. Evaluation of wearing course mix designs on sound absorption improvement of porous asphalt pavement. *Constr. Build. Mater.* **2017**, *141*, 402–409. [CrossRef]
36. Liu, M.; Huang, X.M.; Xue, G.Q. Effects of double layer porous asphalt pavement of urban streets on noise reduction. *Int. J. Sustain. Built Environ.* **2016**, *5*, 183–196. [CrossRef]
37. Knabben, R.M.; Trichês, G.; Gerges, S.N.Y.; Vergara, E.F. Evaluation of sound absorption capacity of asphalt mixtures. *Appl. Acoust.* **2016**, *114*, 266–274. [CrossRef]
38. Zou, L. Research on thermal physical parameters of asphalt mixture. Master's Thesis, Chang'an University, Xi'An, China, 2011.
39. Kassem, E.; Grasley, Z.C.; Masad, E. Viscoelastic Poisson's ratio of asphalt mixtures. *Int. J. Geomech.* **2013**, *13*, 162–169. [CrossRef]
40. Bezemer-Krijnen, M.; Wijnant, Y.H.; de Boer, A. Predicting sound absorption of stacked spheres: Combining an analytical and numerical approach. *Acta. Acust. United. Acust.* **2016**, *102*, 971–983. [CrossRef]